Opto-Electronic Advances

CN 51–1781/TN ISSN 2096–4579 (Print) ISSN 2097–3993 (Online)

Coulomb attraction driven spontaneous molecule-hotspot pairing enables universal, fast, and large-scale uniform single-molecule Raman spectroscopy

Lihong Hong, Haiyao Yang, Jianzhi Zhang, Zihan Gao and Zhi-Yuan Li

Citation: Hong LH, Yang HY, Zhang JZ, et al. Coulomb attraction driven spontaneous molecule-hotspot pairing enables universal, fast, and large-scale uniform single-molecule Raman spectroscopy. *Opto-Electron Adv* **8**, 240309(2025).

https://doi.org/10.29026/oea.2025.240309

Received: 22 December 2024; Accepted: 16 May 2025; Published online: 9 July 2025

Opto-Electronic Advances

Article

July 2025, Vol. 8, No. 7

DOI: 10.29026/oea.2025.240309 CSTR: 32247.14.oea.2025.240309

Coulomb attraction driven spontaneous molecule-hotspot pairing enables universal, fast, and large-scale uniform single-molecule Raman spectroscopy

Lihong Hong[1,2†], Haiyao Yang[1†], Jianzhi Zhang[1], Zihan Gao[1] and Zhi-Yuan Li[1,3*]

Raman spectroscopy offers a great power to detect, analyze and identify molecules, and monitor their temporal dynamics and evolution when combined with single-molecule surface-enhanced Raman scattering (SM-SERS) substrates. Here we present a SM-SERS scheme that involves simultaneously giant chemical enhancement from WS_2 2D materials, giant electromagnetic enhancement from plasmonic nanogap hot spot, and inhibition of molecular fluorescence influence under near-infrared laser illumination. Remarkably we find Coulomb attraction between analyte and gold nanoparticle can trigger spontaneous formation of molecule-hotspot pairing with high precision, stability and robustness. The scheme has enabled realization of universal, robust, fast, and large-scale uniform SM-SERS detection for three Raman molecules of rhodamine B, rhodamine 6G, and crystal violet with a very low detection limit of 10^{-16} M and at a very fast spectrum acquisition time of 50 ms.

Keywords: single-molecule Raman spectroscopy; Coulomb attractions; electromagnetic enhancement; chemical enhancement; near-infrared laser illumination

Hong LH, Yang HY, Zhang JZ et al. Coulomb attraction driven spontaneous molecule-hotspot pairing enables universal, fast, and large-scale uniform single-molecule Raman spectroscopy. *Opto-Electron Adv* **8**, 240309 (2025).

Introduction

Raman spectroscopy is a traditional powerful means to observe vibrational, rotational, and other low-frequency modes in molecules, solids, and two-dimensional materials via inelastic scattering against light, and enable molecule and material analysis and identification[1–4]. It is highly desirable to probe Raman signal with ultrahigh spectroscopic sensitivity down to single-molecule detection level, where the Raman scattering signal strength is comparable with much more sensitive fluorescence signal intensity. This capability of single-molecule Raman spectroscopy (SM-RS) would allow one to probe, analyze, identify, monitor, and manipulate single molecules more deeply and precisely both in temporal and spectral domains and explore better applications in basic

[1]School of Physics and Optoelectronics, South China University of Technology, Guangzhou 510640, China; [2]Institute of Physics, Henan Academy of Sciences, Zhengzhou 450046, China; [3]State Key Laboratory of Luminescent Materials and Devices, South China University of Technology, Guangzhou 510640, China.

†These authors contributed equally to this work.

*Correspondence: ZY Li: phzyli@scut.edu.cn

Received: 22 December 2024; Accepted: 16 May 2025; Published online: 9 July 2025

sciences and high technology in chemistry, biology, medicine, agriculture, food, environment, and drug[5–12]. Besides, SM-RS is not just an ultrasensitive version of traditional Raman spectroscopy, but rather opens up a new window to observe subtle spectroscopic phenomena in single molecule without statistical average, enabling much more clarified observation of molecule science details[13,14]. Unfortunately, as inelastic Raman scattering is a high-order light-matter interaction process compared with fluorescence and Rayleigh scattering, the intrinsic interaction cross-section and extrinsic scattering signal intensity is extremely low and weak, very delicate strategies must be explored for serving this fundamental goal.

In the past 50 years, some technological schemes, with surface-enhanced Raman spectroscopy (SERS) being the most prominent one[15–24], have been implemented to advance Raman spectroscopy in both signal enhancement and detection sensitivity. Two most prestigious physical and chemical mechanisms of Raman enhancement, the electromagnetic enhancement (EME) and chemical enhancement (CME), have played a pivotal role. EME is mainly induced by mesoscopic local surface plasmon resonance (LSPR) effect in metallic nanoparticles and nanostructures with their free electron gas violently interacting with incident laser light, leading to occurrence of great electric field intensity and Raman enhancement in specific nanoscale regions called hot spot[15–24]. CME is mainly a microscopic effect where the molecule Raman cross section (or Raman activity) is enlarged by the formation of loose chemical bond between molecule and surrounding background and consequent action of additional pathways of charge-transfer resonance[25–32]. Other mechanisms, like plasmon amplification via gain[33] and Rayleigh-Raman collective action[34,35], have also been proposed to further enhance Raman signal.

It is generally acknowledged that all these contemporary macroscopic, mesoscopic, and microscopic strategies of Raman enhancement, when they only play separately, are hard to reach the huge enhancement factor (EF) of ~14–15 orders of magnitude so that the Raman signal intensity is comparable with molecule fluorescence to reach SM-RS via SM-SERS[36–39]. Fortunately, when two or more of these strategies act collectively, synergistically, and constructively, things can become very much inspiring[40–42]. A recent experimental work[43] has explored the synergic action of both EME and CME, designed a 2D material-Au plasmonic nanogap SM-SERS substrate for rhodamine B (RhB) molecule, and implemented Raman spectroscopy with an extremely low detection limit and an extremely high statistical EF. The EME coming from the plasmonic nanogap hot spot contributes a giant 9–11 orders of magnitude EF and the CME originating from the transition-metal dichalcogenide WS_2 single layer contributes another giant 4–5 orders of magnitude EF.

Yet, a series of critically important while badly understood issues concerning this synergic EME-CME SM-SERS scheme deserve for good answers: 1) How is the analyte molecules bound to WS_2 absorbed into the plasmonic nanogap to appreciate both giant EME and giant CME? 2) How robust is this route? 3) Can the scheme be extensible to other analyte molecules? 4) Are the SM-SERS active sites are uniformly distributed in large area? 5) How stable is the analyte molecule under laser illumination? 6) How fast is the speed to acquire a Raman spectrum with sufficiently good profile and signal-to-noise ratio (SNR)? In the current work, we wish to answer these questions and find a route towards further optimizing and advancing the great power of this synergic EME-CME SM-SERS scheme. We will show that by using 785 nm laser as illumination source, the WS_2-Au nanosystem can become a universal, robust, fast, and uniform SM-SERS substrate for three typical Raman molecules of RhB, rhodamine 6G (R6G), and crystal violet (CV).

Results and discussions

Definitive formation of molecule-hotspot pairing via Coulomb attraction

The SM-SERS substrate for RhB, R6G, and CV includes three ingredients, as schematically illustrated in Fig. 1(a). One is the plasmonic nanogap formed by Au nanosphere particles (see Fig. 1(b) for geometric configuration details) sitting on a gold thin film mirror sandwiched with a separation SiO_2 layer with a specially designed thickness 2 nm to ensure optimized EME[43], one is the 2D monolayer WS_2 single-crystalline sheet sandwiched between SiO_2 and Au particle (see Fig. 1(c) for geometric configuration details) and offering giant CME. The other is the Raman analyte molecule tightly bound to WS_2 sheet to appreciate giant CME and immersed within the plasmonic hot spot to appreciate giant EME. Note that although the procedure to prepare these SM-SERS substrates is not complicated (**Materials and methods**)[43], it must be sufficiently delicate to ensure WS_2 sheet to

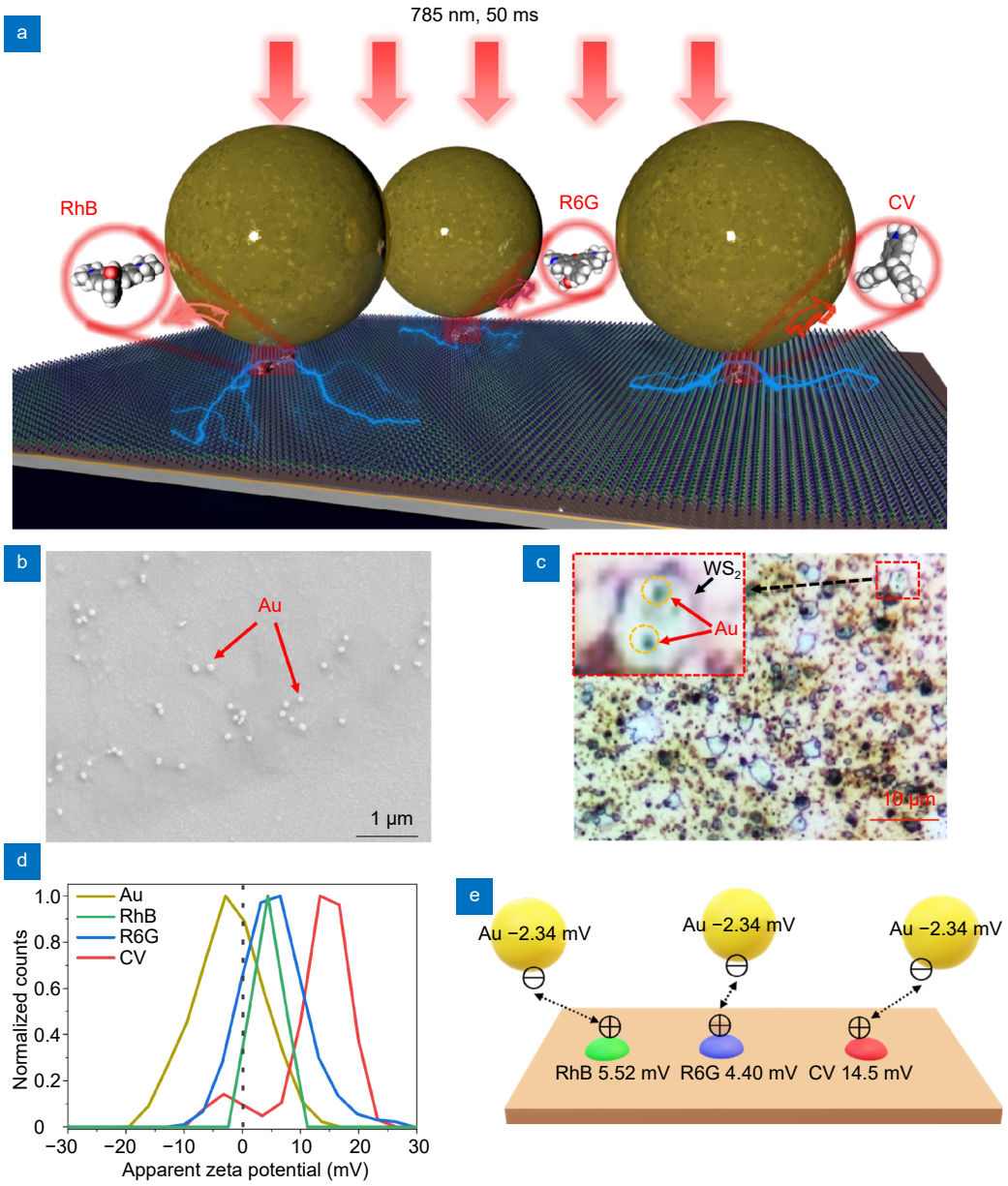

Fig. 1 | Basic structure and working mechanism of SM-SERS substrate. (**a**) Schematic diagram of fast SM-SERS signal formation. (**b**) SEM image of SM-SERS substrate. (**c**) Optical image of the sample under a micro-Raman spectrometer. The area highlighted in the red box is an indication of the area where the gold nanoparticles are bound to the WS_2 2D material. (**d**) Zeta potentiogram of gold nanoparticles and three molecule solutions. (**e**) Schematic illustration of gold nanoparticles approaching to and sitting on WS_2-bound molecules by Coulomb attraction.

insert into the plasmonic nanogap. Nonetheless, there is still one critical issue that stands in the core of the whole SM-SERS scheme, but up to now still remains a puzzling mystery: How is the molecule absorbed right within the nanogap hot spot? Or more precisely in the context of the current preparation process, how does the molecule-particle pair automatically form, so that the molecule can best appreciate the double-fold giant EME and CME? If the Au nanoparticle has already sat on the Au mirror to form a nanogap, then it is very hard, if not impossible, for the analyte molecule to move into the nanogap, as is the case in most SERS experiments involving Au nanoparticles. Or, if the molecule (bound to WS_2 sheet) has already sat on the Au mirror and if the Au particle randomly sits on the Au mirror, then the probability for an Au particle to sit right above a molecule is very low, if not zero. Or, if both molecule and particle are free in water solution, then the probability for them to bind together and form the best geometry of Au particle sitting right on molecule is also very low. Obviously, there must

be some unusual, delicate and magnificent, but unfortunately unknown physical/chemical mechanism to have molecules and particles form one-to-one pair in the configuration illustrated in Fig. 1(a).

We have conjectured that some certain Coulomb attraction forces between the molecules and particles have played into crucial action in this process. To confirm whether this hypothesis is true or not, we use Zeta potentiometric analyzer (Malvern Zetasizer Nano ZS90) to measure the Zeta potential of the three molecule solutions and the Au particle solution (Fig. 1(d)). We find that the molecule framework of RhB, R6G, and CV solution shows positive Zeta potential, while the Au particle solution shows negative Zeta potential (Fig. 1(e)). Consequently, when the WS_2 sheet tightly bound molecules are first absorbed solidly on the Au mirror and then meet the Au particle solution, the positively charged molecules (RhB, R6G, and CV) will attract the freely moving negatively charged Au particles to sit right above the molecules and form the right molecule-particle pair plasmonic nanogap configuration (Fig. 1(e)). This molecule-hotspot pairing mechanism obviously is the critical core of the current EME-CME SM-SERS routine.

In our experiment, the single-layer WS_2 sheet, with a lateral size of 0.1–4.0 μm, has the same density of 0.1 mg/mL in all samples. Simple calculation shows that the concentration of WS_2 sheet is within the range of 7.44×10^{-10}–4.65×10^{-7} M. In the case of low concentration of analyte molecules ranging from 10^{-12} M to 10^{-16} M considered in the current work, the average number of analyte molecules adsorbed in each WS_2 sheet is considerably lower than 1, and the probability for a WS_2 sheet adsorbing more than 1 molecule is very low. On the other hand, in all SM-SERS samples to form molecule-hotspot pairing structure, the Au particle concentration, which has a total number of about 4×10^7, is much higher than the molecule concentration (10^{-12}–10^{-16} M). Thus, each molecule can find an appropriate Au particle to arrange the molecule-particle pair and implement the molecule-hotspot pairing mechanism with high precision, stability, and robustness in geometric configuration (see Fig. 1(b) for Au nanoparticle SEM picture and Fig. 1(c) for WS_2-Au nanoparticle). Therefore, the microscopic mechanism of Coulomb attraction down to the deepest molecule level will greatly enhance the universality, uniformity, robustness, and stability of synergic EME-CME SM-SERS active sites in the current scheme.

High-speed Raman spectroscopy

Now that we have confirmed that the current preparation scheme of SM-SERS substrate has the unique power to allow for the RhB, R6G, and CV molecules to automatically attract Au particles to form a one-to-one molecule-particle SM-SERS active sites with high precision, stability, and robustness, we proceed to see the capability of Raman signal detection. For good reference, we have measured the Raman signal level of SM-SERS substrate for RhG, R6G, and CV in various solution concentrations, and compared with the Raman signal of these molecules placed upon the surface of a bare silicon wafer without any Raman enhancement, now in much higher concentrations. The results for SM-SERS substrate acquired for a very low concentration of 10^{-16} M with a very fast data collection time of only 50 ms, and for a bare silicon substrate acquired for a much higher concentration of 10^{-3} M and with a much longer data collection time of 1.0 s are displayed in Fig. 2. Here the 785 nm laser has been used to shine and excite Raman spectroscopy (**Materials and methods**). It can be estimated from the comparison data that the statistical EF number for the SM-SERS substrate is 4×10^{14} for CV (Fig. 2(a) and 2(b)), 4×10^{14} for R6G (Fig. 2(c) and 2(d)), and 2×10^{15} for RhB (Fig. 2(e) and 2(f)). Obviously all the three SM-SERS substrates have entered deeply into the realm of SM Raman detection, since the Raman cross section is comparable with the fluorescence cross section for the three molecules.

Notice that the excitation laser is a near infrared (NIR) laser of wavelength 785 nm, which is well longer than the absorption band of RhB, R6G, and CV molecules and thus cannot excite fluorescence that always exists in ordinary cases of short excitation wavelength like 514, 532, and 633 nm. In the current scheme, the disturbing problem of fluorescence background contamination to the Raman signal and a degraded signal to noise contrast (SNR) can be completely avoided. The advantage of using the case of 785 nm NIR pump laser against the usual 532 nm pump laser for RhB can be clearly envisioned from Fig. S1 (Supplementary information). Obviously, the fluorescence baseline signal level at the 532 nm pump laser is much higher than the Raman signal (Fig. S1(a)). Only when this baseline signal is subtracted does the true Raman spectrum profile show up, but with a signal-to-noise level much lower than in the 785 nm laser pumping (Fig. S1(b)). Even more surprisingly, the 785 nm pump laser brings about a much higher (~100 times

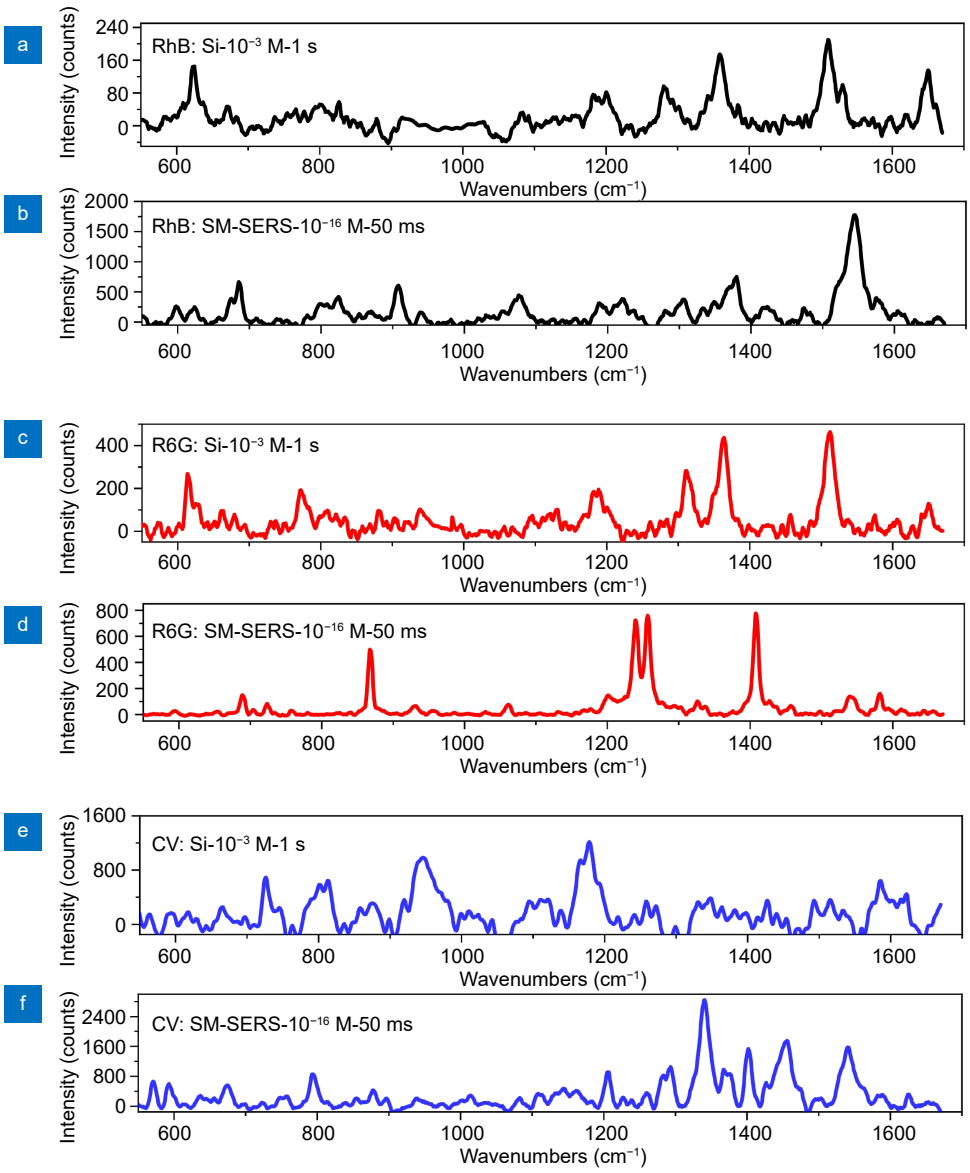

Fig. 2 | Universal enhancement power of SM-SERS substrate on Raman signals for three molecules in comparison with reference silicon substrate. (**a**) Raman spectrum of RhB. (**b**) Fast SM-SERS spectrum of RhB. (**c**) Raman spectrum of R6G. (**d**) Fast SM-SERS spectrum of R6G. (**e**) Raman spectrum of CV. (**f**) Fast SM-SERS spectrum of CV. The ordinary Raman spectrum is made in a silicon substrate for 10^{-3} M analyte concentration and with 1 second signal acquisition time, while the SM-SERS spectrum is implemented for 10^{-16} M analyte concentration and with 50 ms signal acquisition time.

stronger) Raman signal intensity compared with the 532 nm pump laser. This comparison study indicates that the inhibition of fluorescence background signal greatly enhances the Raman spectroscopy sensitivity level and could become a good supplemental route to advance the power of SERS to evolve into the realm of SM-SERS. This advantageous feature, together with the double-fold giant CME from the WS_2 single atomic layer and giant EME from plasmonic nanogap hot spot that is intrinsically offered by the 2D material-molecule-Au particle substrate[43], brings about a powerful capability of universal, fast, and robust SM Raman spectroscopy detection.

As shown in Fig. S1, a series of major Raman peaks are clearly seen. We have used M1-M6 to mark the C–C–C bending, C–H bending, C–H wiggling, C–N stretching, C–C stretching, and aromatic C=C stretching vibration mode of RhB molecule, respectively. The vibration modes corresponding to all the major Raman peaks have been identified and directly marked. Due to low background signal at 785 nm excitation, all the Raman peaks of M1–M6 modes are clearly visualized, while the bad SNR at the 532 nm excitation makes it hard to read out

the low-wavenumber M1–M3 modes. This again confirms the importance to inhibit the fluorescence background when the analyte is at a very low concentration (say, 10^{-14} M).

Large-scale high-uniformity SM-SERS demonstrations

We proceed to perform a large-scale Raman mapping using the micro-Raman spectroscopy instrument across the whole sample of size 5 mm × 5 mm, upon which altogether 30 μL solution of WS_2-bound molecules is dropped (**Materials and methods**). Even after spinning operation, the concentration is higher in the center region than in the edge region. The results for two ultra-low concentration values as 10^{-14} M and 10^{-16} M are displayed in Fig. 3 for RhB, R6G, and CV. For 10^{-16} M concentration, the total number of molecules is 1800, while for 10^{-14} M concentration this number is 180,000. It can be readily calculated that at 10^{-12} M concentration, each 1 μm × 1 μm detection area of Raman instrument laser spot contains approximately 0.72 dye molecules, making 10^{-12} M to 10^{-11} M the concentration range just go across the door of single-molecule detection regime for RhB, R6G, and CV using our SERS substrate system. Thus, the 10^{-14} M and 10^{-16} M concentrations have well exceeded the single molecule detection limit. For each molecule and each concentration, the Raman mapping graph within a specially selected zone of size 60 μm × 90 μm is shown here, where the scanning step is 1 μm and the Raman spectroscopy data acquisition speed is 50 ms per scanning point, a very fast Raman mapping speed. Only those points with considerably high Raman count levels are marked by thick red dots. It can be seen that in each microzone, the Raman active sites are very dilute, with the number being 3–4 at 10^{-16} M and 10–20 at 10^{-14} M, respectively. In comparison, the theoretical average number of molecules in such a microzone is 0.4 and 40.0, quietly different from the measured Raman active site number. This is understandable as the solution is in an extremely low concentration level: some regions have one or more molecules, while other regions have no molecules at all. It can be judged that the probability that two or more molecules aggregate and bind together is even more extremely low in this low concentration situation.

We examine the Raman mapping at various concentration levels ranging from 10^{-16} M to 10^{-12} M. The results for RhB are shown in Fig. 4. At each concentration three microzones of size 60 μm × 90 μm are randomly selected. The points with considerably high Raman count levels are also marked by thick red dots to ensure clarity of eyeview. One can find that when the concentration increases, the number of Raman active site grows obviously from 3–6, to 6–10, 8–13, 54–86, and to 127–197, but not in linear proportion to the molecule solution concentration level. This feature again can be understood from the irregular distribution of molecule across the entire 5 mm × 5 mm plate. Besides, the SM-SERS active site

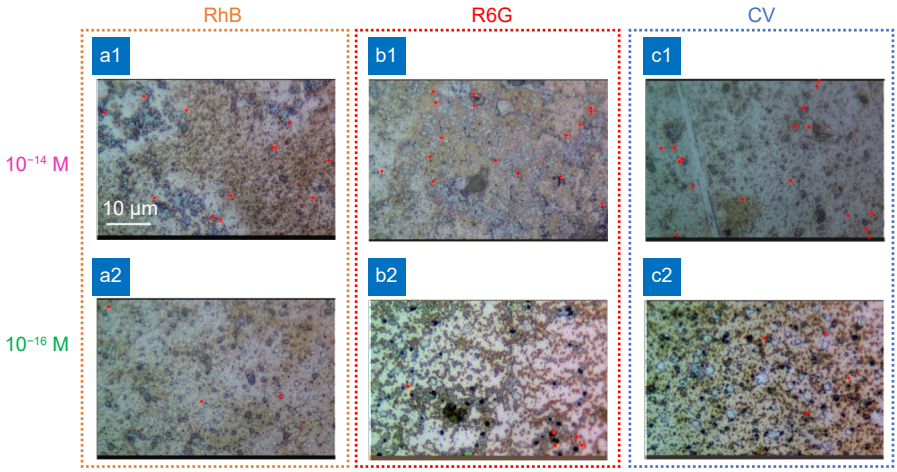

Fig. 3 | Fast SERS scanning imaging of three molecules under ultra-low concentration. The excitation wavelength is 785 nm, the acquisition area is 60 μm × 90 μm, the scanning step length is 1 μm, and the integration time at each point is 50 ms. The sample with 10^{-14} M and 10^{-16} M concentration is shown and compared. (**a1**–**a2**) Fast SERS images of RhB. (**b1**–**b2**) Fast SERS images of R6G. (**c1**–**c2**) Fast SERS images of CV. The optical microscope imaging graphs of the selected-zone sample including WS_2 sheets and Au nanoparticles are also displayed and placed as the background of Raman imaging picture to facilitate better visual conception of the molecular Raman active sites (red dots). The scale bar is 10 μm and applies to all panels.

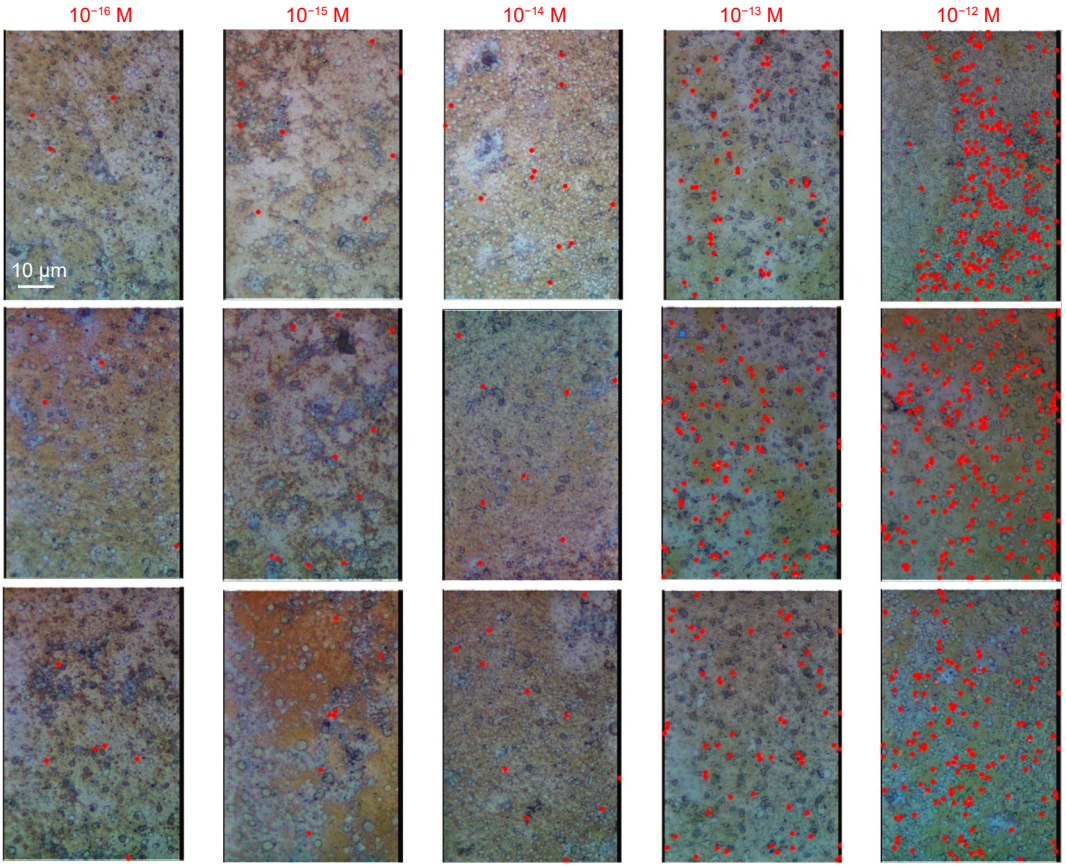

Fig. 4 | Large-scale high-uniformity SERS Raman imaging for RhB molecule. From left to right, the fast SERS images of RhB samples with different concentrations are shown, and from top to bottom, the fast SERS images in three different areas of the same sample are shown. The optical microscope imaging graphs of the selected-zone sample are also displayed and placed as the background of Raman imaging picture. The scale bar is 10 μm and applies to all panels.

number (~200) is far smaller than the molecule number (~4000) at a high concentration level of 10^{-12} M. This indicates that most molecules are not absorbed in WS_2 sheet. On the other hand, the concentration of Au nanoparticle is 0.05 mg/mL, or 10^7 μL^{-1}. This means that at each 5 mm × 5 mm sample plate the total number of Au nanoparticle (with 4 μL in volume) is 4×10^7, indicating average 1.6 Au nanoparticles per square micrometer. Thus, in all concentration of molecules from 10^{-12}–10^{-16} M, the Au nanoparticle concentration is far larger than the molecule concentration.

To understand the component quantity relationships in the SM-SERS base, we mention that the flake size of monolayered WS_2 ranges from 0.1 μm to 4.0 μm. Due to the limitations of current preparation processes, the shapes, flatness, and defects of different fragments vary, leading to significant differences in the adsorption of molecules and the chemical enhancement capabilities of WS_2 monolayer flakes. Moreover, the interactions between the materials themselves can cause stacking and deformation of the flakes. Additionally, a considerable portion of molecules do not adsorb onto the 2D materials but remain free in the solvent. At the same time, although gold nanoparticles have a tendency to be attracted by molecules, some are also scattered in positions without molecules. Finally, the molecules bound to the bottom surface of WS_2 sheet (with a probability 50% compared with those bound to the upper surface) does not impose Coulomb interaction to attract Au particles. Therefore, the number of hot spots that ultimately emit effective Raman signals is much less compared to the number of added molecules.

To further make sure all the Raman active sites are indeed SM-SERS site involving only one molecule when at the ultra-low concentration level of molecule solution, we examine more closely the case of 10^{-16} M concentration. We take nine randomly selected microzones, within each of which there appear several Raman active sites (Fig. 5). We then pick up randomly a Raman active site within each microzone (marked by numbers 1–9), and

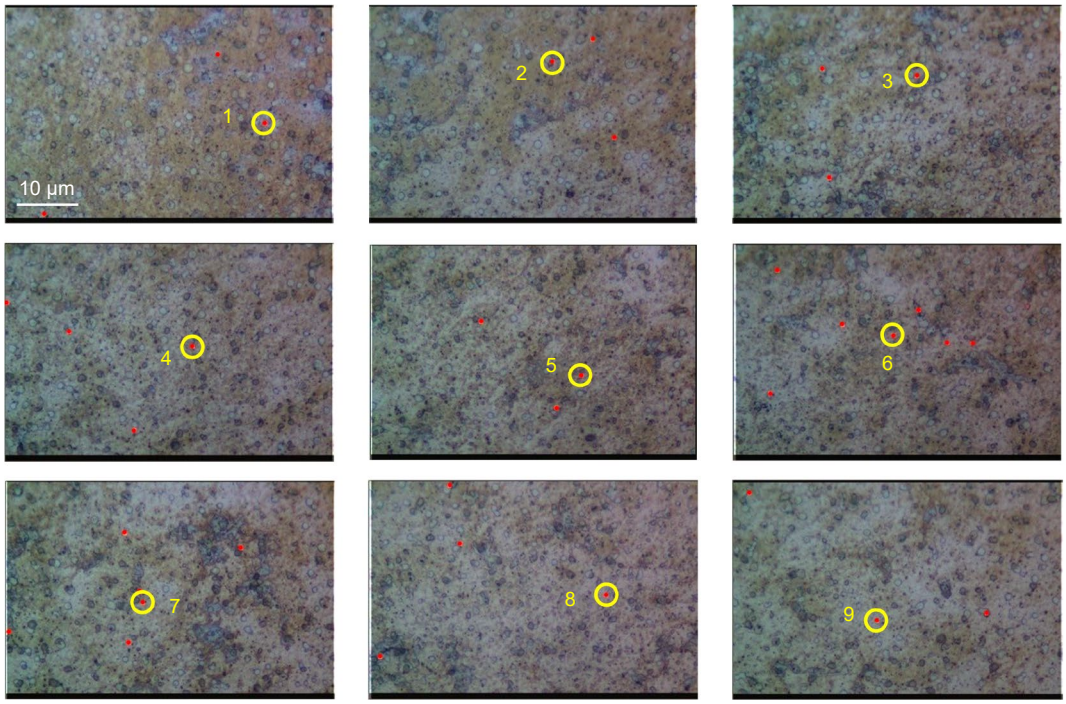

Fig. 5 | Fast SM-SERS images of 10^{-16} M RhB samples in 9 selected regions. For each graph, the Raman spectra of the selected points in the yellow circle are taken to form the following figure of Fig. 6. The optical microscope imaging graphs of the selected-zone sample are also displayed and placed as the background of Raman imaging picture. The scale bar is 10 μm and applies to all panels.

measure their Raman spectra. The results are displayed in Fig. 6. The most noticeable thing is that the Raman signals are on the same count level, indicating all these Raman spectra come from SM-SERS active sites. The second most remarkable thing is that the C–C–C bending, C–H bending, C–H wiggling, C–N stretching, C–C stretching, and aromatic C=C stretching vibration mode for a RhB molecule are clearly visualized. We are able to identify and mark all the major Raman peaks in correspondence to the vibration modes.

Comparison with previous schemes

It is a very remarkable and highly desirable thing that the extremely large Raman signal enhancement down to the SM detection level offered by the current SM-SERS substrate has made it possible to probe and tell unambiguously the variation in the subtle physical and chemical environment around a single molecule via the Raman spectroscopy, a pure optical technology. This powerful capability also holds to the other two analyte molecules as R6G and CV, as can be seen clearly from Figs. S2–S5 (Supplementary information), where the large-scale high-uniformity SM-SERS is obviously illustrated. This once again confirms that the 2D materials, Coulomb attraction and fluorescence inhibition enabled SM-SERS strategy is a universal method towards optically probing, measuring, and monitoring the science of single molecule.

It is interesting and also helpful to compare with previous SERS schemes in terms of Raman enhancement magnitude upper limit and Raman detection sensitivity lower limit. According to numerous previous practices, experiences, and literatures in SERS[15–30], the plasmonic hotpot induced EME has an upper limit of ~10^{10}, the resonant Raman scheme has an upper limit of ~10^{5}, and the charge-transfer resonance induced CME has an upper limit of ~10^{6}. Each of them individually is far away from the ultimate SM goal with Raman signal intensity comparable with fluorescence. Thus, SM-SERS becomes possible only when two or more Raman enhancement routes work collectively and constructively. The most mature scheme of SM-SERS is Au and Ag nanoparticle colloidal aggregates[16,17], which offer a number of nanogap hotspots with giant EME[18]. Together with resonant Raman excitation (offering very large Raman EF)[17] or with NIR laser excitation (offering low fluorescence background)[16], this system has become a classical promising SM-SERS substrate with a Raman signal EF up to 14–15 orders of magnitude[11,16–18]. Yet, due to the random configuration of colloidal aggregates (leading to big

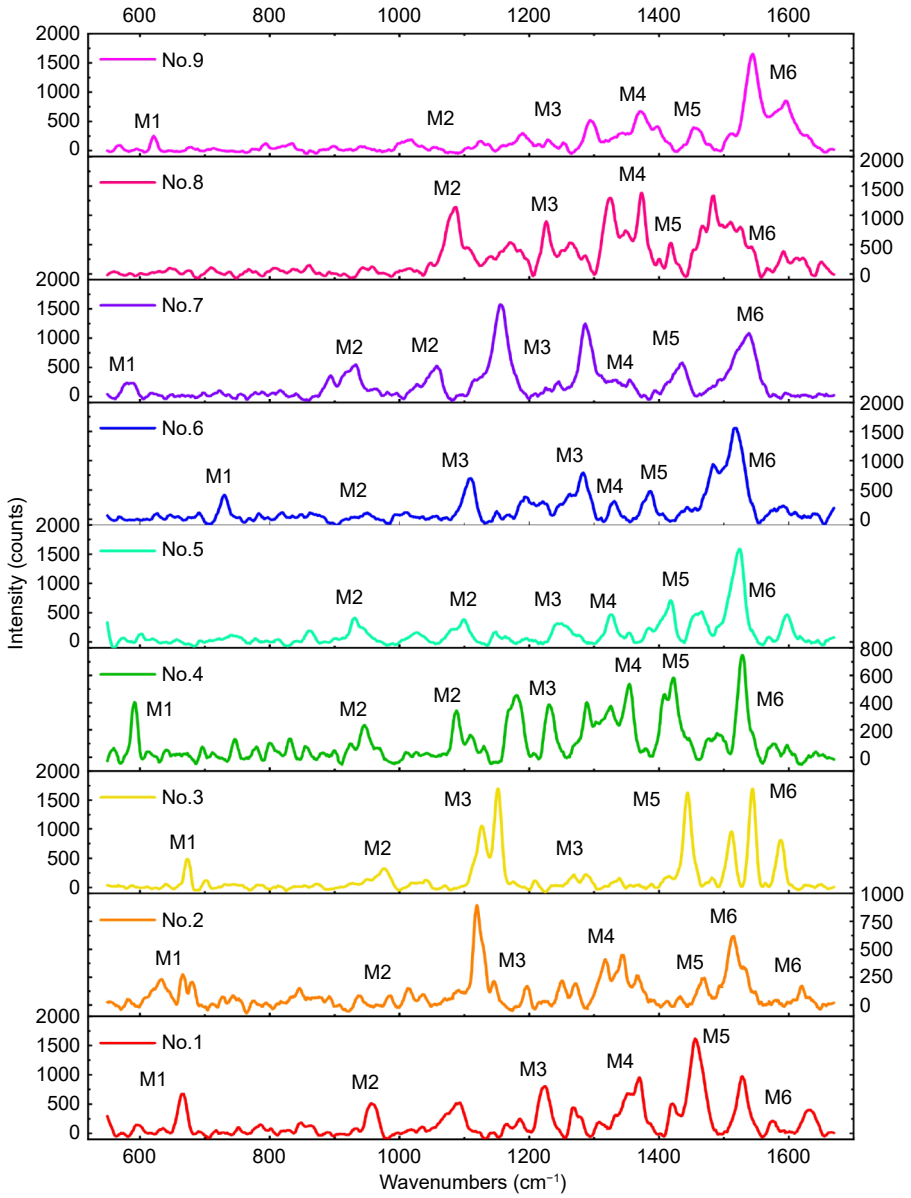

Fig. 6 | SM-SERS spectra of 9 selected points in 10^{-16} M RhB samples. M1–M6 are used to mark the C–C–C bending, C–H bending, C–H wiggling, C–N stretching, C–C stretching, and aromatic C=C stretching vibration mode of RhB molecule, respectively. The vibration modes corresponding to all the major Raman peaks are identified and directly marked.

fluctuations in the EME strength), low probability of analyte molecules to automatically go into the nanogap hotpot (leading to uncertainty of having giant EME), and lack of strong CME mechanism only via Au and Ag materials, this scheme does not provide universal, fast, robust, and large-scale uniform SM Raman spectroscopy detection. In this regard, the current SM-SERS routine enabled by 2D materials offering giant CME, Coulomb attraction offering robust automatic molecule-hotspot pairing to achieve giant EME, and NIR excitation of Raman scattering offering inhibition of fluorescence has incorporated three major Raman enhancement channels and thus it represents a big advancement upon previous SERS and SM-SERS schemes.

Raman spectra of single molecules influenced by environment

According to the simulations illustrated in Figs. S6–S8 (Supplementary information) showing several prominent vibration modes for RhB, R6G, and CV molecules, almost all atoms undergo displacement during each vibrational mode. Each vibrational mode is categorized and organized based on the vibration of its main functional groups. For RhB and R6G molecules, the main

framework consists of a xanthene ring and dye group. Their vibrations can be classified as M1: xanthene ring (XR) C–C–C In-plane bending, M2: methyl C–H bending, M3: C–H in-plane wiggling, M4: C–N stretching, M5: dye group C–C stretching, and M6: aromatic C=C stretching. For CV molecules, which are composed of a benzene ring and dye group, the vibrations are categorized as N1: benzene ring out-of-plane bending, N2: benzene ring in-plane bending, and N3: benzene ring C–H stretching. The Raman peaks displayed in Fig. 2 can be assigned to these feature vibrations, which are comprehensively summarized in Table 1. Besides, from Fig. 2, one can see that the Raman peaks of RhB, R6G, and CV show intensity fluctuations either at high or low concentrations.

Similarly, the Raman peaks displayed in Fig. 6 can also be categorized according to their feature vibrations, and they are comprehensively summarized in Table 2. From Fig. 6, it is evident that the experimental results indicate lateral shifts in the Raman characteristic peaks of RhB. We propose that this variation primarily arises from the following mechanism. First, when RhB molecule enters the hotspot region and interact with the uneven monolayer of WS_2 on the surface, they may produce deformation. This deformation can alter the vibrational frequency of certain chemical bonds, leading to a lateral shift in the position of the Raman peaks. Additionally, there exists a charge transfer process between RhB molecules and WS_2, which influences the redistribution of outer electrons in RhB molecule. This interaction further contributes to the lateral shift observed in the Raman peak positions within the spectrum upon excitation with 785 nm light.

Another remarkable thing is that the vibration modes exhibit some certain differences in terms of Raman peak shift, strength, and profile. This subtle Raman spectral variation can be ascribed to the different environment around the molecule, leading to different physical and chemical interaction with the molecule[44,45]. It can be imagined that there exist a series of physical and chemical configuration variations within the WS_2-molecule-Au nanoparticle nanosystem that can influence the Raman spectroscopy for these molecules. First, when a molecule is absorbed with WS_2 sheet, the spatial orientation of the anisotropic molecule, its binding point with the WS_2 sheet, and the local physical and chemical environment, would be quite different. This would result in difference in charge-transfer efficiency and strength and the corresponding CME on the one hand, and difference in the way the molecules vibrate and the corresponding Raman spectral profile on the other hand[46,47]. Second, the Au spherical nanoparticles, with an average diameter of 80 nm, always have variation in size and shape. When these negatively charged Au nanoparticles are Coulomb attracted to sit right on the positively charged analyte molecules, the subtle plasmon nanogap configuration

Table 1 | Identification and classification of Raman spectra in Fig. 2.

Scan type of SERS	Type of molecule	Raman characteristic peaks (cm^{-1})
Si-10^{-3} M-1 s	RhB	625 (M1), 1181 (M3), 1200 (M3), 1280 (M3), 1359 (M4), 1510 (M5), and 1649 (M6)
SM-10^{-16} M-50 ms	RhB	685 (M1), 908 (M2), 1075 (M2), 1380 (M4), and 1544 (M6)
Si-10^{-3} M-1 s	R6G	613 (M1), 771 (M1), 1188 (M3), 1311 (M4), 1364 (M4), 1512 (M5), and 1649 (M6)
SM-10^{-16} M-50 ms	R6G	688 (M1), 867 (M2), 1239 (M3), 1356 (M4), 1408 (M4), and 1582 (M6)
Si-10^{-3} M-1 s	CV	726 (N1), 812 (N1), 946 (N1), 1178 (N2), 1586 (N3), and 1622 (N3)
SM-10^{-16} M-50 ms	CV	674 (N1), 793 (N1), 1205 (N2), 1340 (N2), 1401 (N2), 1455 (N2), and 1540 (N3)

Table 2 | Identification and classification of SM-SERS spectra of 9 selected points in Fig. 6.

Regions	Type of molecule	Raman characteristic peaks (cm^{-1})
No.9	RhB	619 (M1), 1020 (M2), 1190 (M3), 1293 (M3), 1371 (M4), 1453 (M4), 1544 (M5), 1595 (M6)
No.8	RhB	1086 (M2), 1226 (M3), 1324 (M4), 1373 (M4), 1416 (M5), 1484 (M5), 1591 (M6)
No.7	RhB	583 (M1), 932 (M2), 1057 (M2), 1155 (M3), 1286 (M3), 1371 (M4), 1445 (M5), 1548 (M6)
No.6	RhB	712 (M1), 953 (M2), 1110 (M2), 1283 (M3), 1386 (M4), 1483 (M5), 1517 (M6)
No.5	RhB	930 (M2), 1099 (M2), 1258 (M3), 1325 (M4), 1418 (M5), 1524 (M5), 1596 (M6)
No.4	RhB	591 (M1), 945 (M2), 1087 (M2), 1180 (M3), 1230 (M3), 1288 (M3), 1325 (M4), 1422 (M4), 1530 (M5), 1598 (M6)
No.3	RhB	673 (M1), 976 (M2), 1126 (M2), 1193 (M3), 1182 (M3), 1444 (M4), 1512 (M5), 1544 (M5), 1587 (M6)
No.2	RhB	633 (M1), 1119 (M2), 1317 (M4), 1342 (M2), 1515 (M6), 1619 (M6)
No.1	RhB	664 (M1), 956 (M2), 1092 (M2), 1224 (M3), 1370 (M4), 1455 (M5), 1528 (M6), 1633 (M6)

and the relative position of the molecule within the nanogap would be different. This subtle molecule-nanogap geometric configuration variation would cause subtle difference in the molecule-hotspot optical interaction strength and the corresponding EME.

Conclusions and perspectives

In this work, we have presented a SM-SERS scheme that involves a 2D materials WS_2 single layer inserted into the plasmonic nanogap hotspot formed between an Au nanoparticle sitting on a flat Au mirror. We have explored, discovered, and harnessed three major mechanisms that collectively, synergistically and constructively act to push up the Raman EF for three general Raman analyte molecules, RhB, R6G, and CV, to an extremely large level as 14–15 orders of magnitude, well going into the SM-SERS realm. First, Coulomb attraction can help to trigger negatively charged Au nanoparticle automatically absorbed upon positively charged molecules tightly bound to WS_2 to form spontaneous molecule-hotspot pairing with high precision, stability and robustness and offer giant EME from plasmonic nanogap. Second, the WS_2 single atomic layer inserted into the plasmonic nanogap can offer an efficient and broad charge transfer channel for tightly bound analyte molecules and lead to giant CME. Third, the NIR laser used to excite Raman scattering can efficiently inhibit molecular fluorescence background signal in contamination to Raman signal and lead to high SNR. These three major advantageous measures act together positively and collectively to realize universal, robust, fast, and large-scale uniform SM-SERS detection for RhB, R6G, and CV with a detection limit of 10^{-16} M and a spectrum acquisition time of 50 ms.

The 2D materials, Coulomb attractions, and fluorescence inhibition synergistic SM-SERS scheme could arm scientists with a powerful capability of optically probing and monitoring the spatial-temporal evolution of the physical, chemical, and biological properties of molecules, and thus it would open up a new frontier of molecular science. The current scheme, although only demonstrated to act upon the RhB, R6G, and CV molecules as Raman analytes, Au nanoparticles EME agents, and WS_2 as CME agents, can be extended to other more general molecules and metal nanoparticles (upon which positive and negative charges can be imposed), and 2D materials (to be designed in match with a specific Raman analyte for considerable CME). Moreover, the current scheme can be combined with the contemporary well-developed large-scale TMD 2D materials production and transfer technique and thus is ready for expanding into an even larger-scale SM-SERS chip of several inches in size. Finally, this powerful SM-SERS technology can also be incorporated with the mature microfluid chip technology to offer a cheap and versatile platform for implementing high-throughput, fast, large-scale biomedical detection via Raman spectroscopy.

Finally, we believe our experimental results have satisfactorily answered the series of questions that we have raised in the beginning of this paper and are of critical importance for the research field of SM-SERS detection. In short, we have elucidated the Coulomb attraction between analyte molecules and Au nanoparticles is the principal mechanism governing how analyte molecules bound to WS_2 sheet are incorporated into plasmonic nanogaps and create optimal EME-CME synergic enhancement regions. We have confirmed the robustness of this approach through consistent generation of distinct, quantity-dependent signal hotspots across multiple samples. The powerful amplification capabilities of our substrate enable stable measurements even after multiple tests, with the remarkably short acquisition times mentioned (50 ms) maintaining good SNR. By systematically addressing these fundamental questions, we have not only developed an effective SERS platform but also advanced understanding of the mechanisms underlying synergic EME and EME in hybrid nanosystems. These findings provide valuable insights for the design of next-generation molecular sensing technologies and open exciting possibilities for applications in various fields of single-molecule physics, chemistry and biology.

Materials and methods

Materials

Rhodamine B, rhodamine 6G and crystal violet were purchased from Shanghai Adamas Reagent Co., Ltd and used as received. All other chemicals used were reagent grade unless otherwise specified. Mono-layer WS_2 dispersion was fabricated by Nanjing Muke Nano-Tech. Co., Ltd. Gold nanoparticle colloid was synthesized by Nanjing Xianfeng Nano-Materials Tech Co., Ltd. The 5 mm × 5 mm silicon slices were prepared by Zhejiang Lijing Tech. Co., Ltd. The gold, chromium and SiO_2 sputtering target were acquired from Beijing Dream Material Technology Co., Ltd. Purified water was offered by

Hangzhou Wahaha Group Co., Ltd and used throughout the study.

Instruments and measurements

The SEM image was shot by a GemniSEM 500 electron microscope. The gold, chromium and SiO_2 coating on the SM Raman base were sputtered by an MSP-300B magnetron sputtering instrument. The thickness of coatings was measured by a Bruker DektakXT step profiler. The Zeta potential of RhB, R6G, CV and Au particle solution were measured by a Malvern Nano ZS90 Zetasizer. All the Raman spectra were gained from a Renishaw inVia Raman spectrometer: laser: 785 nm edge (mode: regular), grating: 1200 l/mm (633/785 nm), exposure time for each point: 0.05 s, laser power: 2.5 mW, slit opening: 65 μm, objective: ×100 L; laser: 532 nm edge (mode: confocal), grating: 2400 l/mm (vis), exposure time for each point: 0.5 s, laser power: 2.5 mW, slit opening: 20 μm, objective: ×100 L.

Fabrication of the SM-SERS base

20 nm chromium, 300 nm gold and 2 nm SiO_2 were sputtered on a 5 mm × 5 mm square silicon slice, successively. 0.2 mL WS_2 (0.1 mg/mL) dispersion was mixed with 2.8 mL RhB (R6G or CV) solution with specific concentration (10^{-12}–10^{-16} M), the mixture was ultrasonic stirred for 30 minutes to ensure the molecules absorbed adequately by the 2D material. Afterwards, 30 μL of the mixture was dropped uniformly on the coated slice. After 2 hours vacuum drying under 40 °C, 40 μL 80 nm-diameter gold nanoparticle (50 μg/mL) colloid is added on the aforementioned slice. Eventually, via 2 hours vacuum drying beyond 40 °C, the SM-SERS base can be created. DI water was used as the solvent to disperse Au NPs and WS_2 during the whole experiment.

Fabrication of the reference samples

10^{-3} M RhB (R6G or CV) solution was ultrasonic stirred for 30 minutes. Afterwards, 30 μL of the solution was dropped uniformly on bare silicon plate. Finally, the samples were 2 hours vacuum dried under 40 °C.

References

1. Raman CV, Krishnan KS. A new type of secondary radiation. *Nature* **121**, 501–502 (1928).
2. Lapp M, Penney CM. *Laser Raman Gas Diagnostics* (Springer, New York, 1974).
3. Moskovits M. Surface-enhanced spectroscopy. *Rev Mod Phys* **57**, 783–826 (1985).
4. Aroca R. *Surface-Enhanced Vibrational Spectroscopy* (John Wiley & Sons, Hoboken, 2006).
5. Ferrari AC, Basko DM. Raman spectroscopy as a versatile tool for studying the properties of graphene. *Nat Nanotechnol* **8**, 235–246 (2013).
6. Schlücker S. Surface-enhanced Raman spectroscopy: concepts and chemical applications. *Angew Chem Int Ed* **53**, 4756–4795 (2014).
7. Sharma B, Frontiera RR, Henry AI et al. SERS: materials, applications, and the future. *Mater Today* **15**, 16–25 (2012).
8. Zong C, Xu MX, Xu LJ et al. Surface-enhanced Raman spectroscopy for bioanalysis: reliability and challenges. *Chem Rev* **118**, 4946–4980 (2018).
9. Senga R, Lin YC, Morishita S et al. Imaging of isotope diffusion using atomic-scale vibrational spectroscopy. *Nature* **603**, 68–72 (2022).
10. Wang YH, Zheng SS, Yang WM et al. In situ Raman spectroscopy reveals the structure and dissociation of interfacial water. *Nature* **600**, 81–85 (2021).
11. Bi XY, Czajkowsky DM, Shao ZF et al. Digital colloid-enhanced Raman spectroscopy by single-molecule counting. *Nature* **628**, 771–775 (2024).
12. Ghosh P, Alvertis AM, Chowdhury R et al. Decoupling excitons from high-frequency vibrations in organic molecules. *Nature* **629**, 355–362 (2024).
13. Zhang R, Zhang Y, Dong ZC et al. Chemical mapping of a single molecule by Plasmon-enhanced Raman scattering. *Nature* **498**, 82–86 (2013).
14. Lee J, Crampton KT, Tallarida N et al. Visualizing vibrational normal modes of a single molecule with atomically confined light. *Nature* **568**, 78–82 (2019).
15. Jeanmaire DL, Van Duyne RP. Surface Raman spectroelectrochemistry: part I. Heterocyclic, aromatic, and aliphatic amines adsorbed on the anodized silver electrode. *J Electroanal Chem Interfacial Electrochem* **84**, 1–20 (1977).
16. Kneipp K, Wang Y, Kneipp H et al. Single molecule detection using surface-enhanced Raman scattering (SERS). *Phys Rev Lett* **78**, 1667–1670 (1997).
17. Nie SM, Emory SR. Probing single molecules and single nanoparticles by surface-enhanced Raman scattering. *Science* **275**, 1102–1106 (1997).
18. Xu HX, Bjerneld EJ, Käll M et al. Spectroscopy of single hemoglobin molecules by surface enhanced Raman scattering. *Phys Rev Lett* **83**, 4357–4360 (1999).
19. Li JF, Huang YF, Ding Y et al. Shell-isolated nanoparticle-enhanced Raman spectroscopy. *Nature* **464**, 392–395 (2010).
20. Zrimsek AB, Chiang N, Mattei M et al. Single-molecule chemistry with surface- and tip-enhanced Raman spectroscopy. *Chem Rev* **117**, 7583–7613 (2017).
21. Langer J, de Aberasturi DJ, Aizpurua J et al. Present and future of surface-enhanced Raman scattering. *ACS Nano* **14**, 28–117 (2020).
22. Neumann C, Reichardt S, Venezuela P et al. Raman spectroscopy as probe of nanometre-scale strain variations in graphene. *Nat Commun* **6**, 8429 (2015).
23. Li JF, Tian XD, Li SB et al. Surface analysis using shell-isolated nanoparticle-enhanced Raman spectroscopy. *Nat Protoc* **8**, 52–65 (2013).
24. Dzhagan V, Mazur N, Kapush O et al. Self-organized SERS substrates with efficient analyte enrichment in the hot spots.

ACS Omega **9**, 4819–4830 (2024).
25. Ling X, Fang WJ, Lee YH et al. Raman enhancement effect on two-dimensional layered materials: graphene, h-BN and MoS_2. *Nano Lett* **14**, 3033–3040 (2014).
26. Shutov AD, Yi ZH, Wang JZ et al. Giant chemical surface enhancement of coherent Raman scattering on MoS_2. *ACS Photonics* **5**, 4960–4968 (2018).
27. Wang X, Huang SC, Hu S et al. Fundamental understanding and applications of plasmon-enhanced Raman spectroscopy. *Nat Rev Phys* **2**, 253–271 (2020).
28. Shao MR, Ji C, Tan JB et al. Ferroelectrically modulate the Fermi level of graphene oxide to enhance SERS response. *Opto-Electron Adv* **6**, 230094 (2023).
29. Xiao TH, Cheng ZZ, Luo ZY et al. All-dielectric chiral-field-enhanced Raman optical activity. *Nat Commun* **12**, 3062 (2021).
30. Pancorbo PM, Zhang HH, Yu XX et al. Metal-free SERS: where we are now, where we are heading. *Europhys Lett* **136**, 34001 (2021).
31. Majumdar D. 2D material-based surface-enhanced Raman spectroscopy platforms (either alone or in nanocomposite form) — from a chemical enhancement perspective. *ACS Omega* **9**, 40242–40258 (2024).
32. Meng L, Hu S, Xu CJ et al. Surface enhanced Raman effect on CVD growth of WS_2 film. *Chem Phys Lett* **707**, 71–74 (2018).
33. Li ZY, Xia YN. Metal nanoparticles with gain toward single-molecule detection by surface-enhanced Raman scattering. *Nano Lett* **10**, 243–249 (2010).
34. Zhang C, Chen BQ, Li ZY. Optical origin of subnanometer resolution in tip-enhanced Raman mapping. *J Phys Chem C* **119**, 11858–11871 (2015).
35. Chen BQ, Zhang C, Li JF et al. On the critical role of Rayleigh scattering in single-molecule surface-enhanced Raman scattering *via* a plasmonic nanogap. *Nanoscale* **8**, 15730–15736 (2016).
36. Li ZY. Mesoscopic and microscopic strategies for engineering Plasmon-enhanced Raman scattering. *Adv Opt Mater* **6**, 1701097 (2018).
37. Yu Y, Xiao TH, Wu YZ et al. Roadmap for single-molecule surface-enhanced Raman spectroscopy. *Adv Photonics* **2**, 014002 (2020).
38. Wang HL, You EM, Panneerselvam R et al. Advances of surface-enhanced Raman and IR spectroscopies: from nano/microstructures to macro-optical design. *Light Sci Appl* **10**, 161 (2021).
39. Peng YS, Lin CL, Long L et al. Charge-transfer resonance and electromagnetic enhancement synergistically enabling MXenes with excellent SERS sensitivity for SARS-CoV-2 S protein detection. *Nano-Micro Lett* **13**, 52 (2021).
40. Liu YH, Qiao SD, Fang C et al. A highly sensitive LITES sensor based on a multi-pass cell with dense spot pattern and a novel quartz tuning fork with low frequency. *Opto-Electron Adv* **7**, 230230 (2024).
41. Wu Y, Sun TY, Shao MR et al. Pyroelectrically driven charge transfer and its advantages on SERS and self‐cleaning property. *Laser Photon Rev* **19**, 2401152 (2025).
42. Kaushik A, Bisht P, Senapati S et al. Ag nanoparticle functionalized vertical WS_2 nanoflakes as SERS substrate for chemical sensing. *Surf Interfaces* **52**, 104951 (2024).
43. Yang HY, Mo HR, Zhang JZ et al. Observation of single-molecule Raman spectroscopy enabled by synergic electromagnetic and chemical enhancement. *PhotoniX* **5**, 3 (2024).
44. Sun CH, Wang ML, Feng Q et al. Surface-enhanced Raman scattering (SERS) study on Rhodamine B adsorbed on different substrates. *Russ J Phys Chem A* **89**, 291–296 (2015).
45. Lin S, Hasi WLJ, Lin X et al. Rapid and sensitive SERS method for determination of Rhodamine B in chili powder with paper-based substrates. *Anal Methods* **7**, 5289–5294 (2015).
46. Turley HK, Hu ZW, Jensen L et al. Surface-enhanced resonance hyper-Raman scattering elucidates the molecular orientation of rhodamine 6G on silver colloids. *J Phys Chem Lett* **8**, 1819–1823 (2017).
47. Yi Z, Yi Y, Luo JS et al. Experimental and simulative study on surface enhanced Raman scattering of rhodamine 6G adsorbed on big bulk-nanocrystalline metal substrates. *RSC Adv* **5**, 1718–1729 (2015).

Acknowledgements

The authors are grateful for the financial support from Science and Technology Project of Guangdong (2020B010190001) and National Natural Science Foundation (12434016).

Author contributions

Z. Y. Li supervised the project. Z. Y. Li, H. Y. Yang, and L. H. Hong conceived and designed the experiments. H. Y. Yang and L. H. Hong prepared the samples and performed the experiments. J. Z. Zhang and Z. H. Gao offered assistance in theoretical calculations. L. H. Hong, H. Y. Yang, and Z. Y. Li provided the theoretical and experimental analysis, and wrote the manuscript. All authors participated in the discussion of results and reviewed the manuscript.

Competing interests

The authors declare no competing financial interests.

Supplementary information

Supplementary information for this paper is available at https://doi.org/10.29026/oea.2025.250309

Scan for Article PDF